
Regularized Shallow Water Equations for Numerical Simulation of Flows with a Moving Shoreline

O. V. Bulatov^a and T. G. Elizarova^b

^a Faculty of Physics, Moscow State University, Moscow, 119991 Russia

^b Institute of Applied Mathematics, Russian Academy of Sciences, Miusskaya pl. 4, Moscow, 125047 Russia

e-mail: telizar@mail.ru

Received June 6, 2015; in final form, August 10, 2015

Abstract—A numerical algorithm for simulating free-surface flows based on regularized shallow water equations is adapted to flows involving moving dry-bed areas. Well-balanced versions of the algorithm are constructed. Test computations of flows with dry-bed areas in the cases of water runup onto a plane beach and a constant-slope beach are presented. An example of tsunami simulation is given.

Keywords: shallow water equations, regularization, finite volume method, well-balanced condition, flow with dry-bed areas, tsunami wave.

DOI: 10.1134/S0965542516040047

INTRODUCTION

The fluid dynamics equations in the shallow water (SW) approximation are widely used in the numerical simulation of free surface flows when the vertical velocity can be neglected (see, e.g., [1, 2]). Examples are flows near a shoreline, whose position can vary due to water runup and rundown, which is accompanied by the formation of dry-bed zones. Specifically, such problems arise in the simulation of tsunamis in nearshore regions [3].

A new numerical algorithm for solving the SW equations was proposed and investigated in [4, 5]. The algorithm is based on SW equations regularized or smoothed over a short time interval. The resulting equations were called *regularized SW equations*. They can also be treated as a version of the quasi-gasdynamic equations in the barotropic approximation, which are used for the numerical simulation of viscous compressible gas flows [6, 7].

A wide variety of one-dimensional test problems computed on the basis of the regularized SW equations can be found in [8]. In [9] the formation of a solitary wave in a circular wind-water tunnel was numerically simulated for the first time with the use of the SW approximation. The solitary wave was formed in the tunnel under the influence of a distributed wind load. It was shown in [10] that a numerical algorithm based on the regularized SW equations can be used to simulate dam break flows over a surface with forward- and backward-facing steps. In [11] the liquid oscillations in a fuel tank of an icebreaker were numerically modeled in various cases of vessel stop caused by its collision with ice and maneuvers in waves. In [12] the formation of Faraday waves caused by vertical oscillations of a vessel with fluid was numerically simulated for the first time in the SW approximation. To simulate the effect of the vessel acceleration on the hydrodynamics of the process, the problems were solved in noninertial frames of reference.

In this paper, a numerical method based on solving the regularized SW equations is extended to flows with a moving boundary associated with the formation of dry-bed zones. Well-balanced versions of the algorithm are presented. The algorithm is tested using two Riemann problems with dry-bed zones forming over a flat bottom and two problems of water runup onto a constant-slope beach. Additionally, numerical results are presented for tsunami runup onto a beach of complex geometry.

1. REGULARIZED SHALLOW WATER EQUATIONS

The SW equations in the form of mass and momentum conservation laws can be written as

$$\frac{\partial h}{\partial t} + \frac{\partial u_x h}{\partial x} + \frac{\partial u_y h}{\partial y} = 0, \quad (1)$$

$$\frac{\partial h u_x}{\partial t} + \frac{\partial}{\partial x} \left(h u_x^2 + \frac{1}{2} g h^2 \right) + \frac{\partial}{\partial y} (h u_x u_y) = h f_x - g h \frac{\partial b}{\partial x} + \frac{\partial \Pi_{xx}^{NS}}{\partial x} + \frac{\partial \Pi_{yx}^{NS}}{\partial y}, \quad (2)$$

$$\frac{\partial h u_y}{\partial t} + \frac{\partial}{\partial x} (h u_x u_y) + \frac{\partial}{\partial y} \left(h u_y^2 + \frac{1}{2} g h^2 \right) = h f_y - g h \frac{\partial b}{\partial y} + \frac{\partial \Pi_{xy}^{NS}}{\partial x} + \frac{\partial \Pi_{yy}^{NS}}{\partial y}. \quad (3)$$

Here, the shear stress tensor components are given by

$$\Pi_{xx}^{NS} = \nu h \left(2 \frac{\partial u_x}{\partial x} - \frac{2}{3} \operatorname{div} \mathbf{u} \right), \quad \Pi_{yy}^{NS} = \nu h \left(2 \frac{\partial u_y}{\partial y} - \frac{2}{3} \operatorname{div} \mathbf{u} \right), \quad (4)$$

$$\Pi_{xy}^{NS} = \Pi_{yx}^{NS} = \nu h \left(\frac{\partial u_y}{\partial x} + \frac{\partial u_x}{\partial y} \right), \quad \operatorname{div} \mathbf{u} = \frac{\partial u_x}{\partial x} + \frac{\partial u_y}{\partial y}. \quad (5)$$

The unknowns in system (1)–(3) are the water height $h(x, y, t)$, which is measured from the given bottom profile $b(x, y)$, and the horizontal velocity components $u_x(x, y, t)$ and $u_y(x, y, t)$. Here, g is the acceleration of gravity, ν is the kinematic viscosity coefficient, and f_x and f_y are the components of external forces.

According to [4, 5], the regularized SW equations (1)–(3) have the form

$$\frac{\partial h}{\partial t} + \frac{\partial j_{mx}}{\partial x} + \frac{\partial j_{my}}{\partial y} = 0, \quad (6)$$

$$\frac{\partial h u_x}{\partial t} + \frac{\partial j_{mx} u_x}{\partial x} + \frac{\partial j_{my} u_x}{\partial y} + \frac{\partial}{\partial x} \left(\frac{g h^2}{2} \right) = h^* \left(f_x - g \frac{\partial b}{\partial x} \right) + \frac{\partial \Pi_{xx}}{\partial x} + \frac{\partial \Pi_{yx}}{\partial y}, \quad (7)$$

$$\frac{\partial h u_y}{\partial t} + \frac{\partial j_{mx} u_y}{\partial x} + \frac{\partial j_{my} u_y}{\partial y} + \frac{\partial}{\partial y} \left(\frac{g h^2}{2} \right) = h^* \left(f_y - g \frac{\partial b}{\partial y} \right) + \frac{\partial \Pi_{xy}}{\partial x} + \frac{\partial \Pi_{yy}}{\partial y}, \quad (8)$$

where

$$h^* = h - \tau \left(\frac{\partial h u_x}{\partial x} + \frac{\partial h u_y}{\partial y} \right). \quad (9)$$

The components of the mass flux density are calculated as

$$j_{mx} = h(u_x - w_x), \quad j_{my} = h(u_y - w_y), \quad (10)$$

where

$$w_x = \frac{\tau}{h} \left(\frac{\partial (h u_x^2)}{\partial x} + \frac{\partial (h u_x u_y)}{\partial y} + g h \frac{\partial (h + b)}{\partial x} - h f_x \right), \quad (11)$$

$$w_y = \frac{\tau}{h} \left(\frac{\partial (h u_x u_y)}{\partial x} + \frac{\partial (h u_y^2)}{\partial y} + g h \frac{\partial (h + b)}{\partial y} - h f_y \right). \quad (12)$$

In contrast to the representation in [4, 5] and by analogy with the corresponding expressions for the quasi-gasdynamical equations in [6, 7], the expressions for Π_{ij} are presented in compact form convenient for numerical implementation:

$$\begin{aligned} \Pi_{xx} &= u_x w_x^* + R^* + \Pi_{xx}^{NS}, & \Pi_{yx} &= u_y w_x^* + \Pi_{yx}^{NS}, \\ \Pi_{xy} &= u_x w_y^* + \Pi_{xy}^{NS}, & \Pi_{yy} &= u_y w_y^* + R^* + \Pi_{yy}^{NS}. \end{aligned} \quad (13)$$

Here, w_x^* , w_y^* , and R^* are defined as

$$\begin{aligned} w_x^* &= \tau h \left(u_x \frac{\partial u_x}{\partial x} + u_y \frac{\partial u_x}{\partial y} + g \frac{\partial(h+b)}{\partial x} - f_x \right), \\ w_y^* &= \tau h \left(u_x \frac{\partial u_y}{\partial x} + u_y \frac{\partial u_y}{\partial y} + g \frac{\partial(h+b)}{\partial y} - f_y \right), \\ R^* &= g\tau h \left(u_x \frac{\partial h}{\partial x} + u_y \frac{\partial h}{\partial y} + h \operatorname{div} \mathbf{u} \right). \end{aligned}$$

The tensor Π_{ij} is asymmetric, but $\Lambda_{ij} = u_j j_{m,i} - \Pi_{ij} + \delta_{ij} \frac{1}{2} g h^2$ remains symmetric; as a result, the equations of motion can be represented as

$$\begin{aligned} \frac{\partial h u_x}{\partial t} + \frac{\partial \Lambda_{xx}}{\partial x} + \frac{\partial \Lambda_{yx}}{\partial y} h^* \left(f_x - g \frac{\partial b}{\partial x} \right), \\ \frac{\partial h u_y}{\partial t} + \frac{\partial \Lambda_{xy}}{\partial x} + \frac{\partial \Lambda_{yy}}{\partial y} h^* \left(f_y - g \frac{\partial b}{\partial y} \right). \end{aligned}$$

In the above expressions, τ is a small parameter of regularization or time smoothing and has the dimension of time. The terms involving τ are regularizing terms for SW equations (1)–(3). When $\tau = 0$, the regularized equations (6)–(8) become the classical SW equations.

Equation (6) contains second spatial derivatives, which leads to a special boundary condition in the formulation of initial–boundary value problems for the regularized SW equations. Specifically, the impermeability condition for system (6)–(8) has the form $\mathbf{j}_m = 0$. In Cartesian coordinates, according to (10)–(12), this condition is written depending on the position of the boundary as

$$u_x = 0, \quad g \frac{\partial}{\partial x} (h + b) = f_x$$

or

$$u_y = 0, \quad g \frac{\partial}{\partial y} (h + b) = f_y.$$

For the regularized SW equations, a balance equation for specific entropy has been derived and it has been established that the specific entropy does not decrease. Thus, it has been shown that the τ -terms are dissipative in nature [13–15]. A linearized system of regularized SW equations was constructed. For it, energy relations were obtained and theorems on the asymptotic stability of an equilibrium solution and on the uniqueness of a classical solution were proved (see [16]). Necessary and sufficient conditions for the non-uniform and uniform Petrovskii parabolicity of the regularized equations were established. The properties of exact solutions of the regularized equations and their relations to exact solutions of the original equations for the barotropic gas dynamics equations and the SW approximation were examined in [14–16]. A method for constructing common exact solutions of the classical and regularized SW equations in the Saint-Venant form was proposed in the stationary case. It was shown that, if $u_x(x, y)$, $u_y(x, y)$, and $h(x, y)$ are the solution of the stationary SW equations, then they are also the solution of the stationary regularized equations.

Specifically, for the regularized SW equations and the original system (1)–(3), the hydrostatic equilibrium condition is satisfied, i.e., for a fluid that is initially at rest ($u_x = u_y = 0$) in the absence of external forces ($f_x = f_y = 0$), the free surface elevation remains a constant at any subsequent time:

$$\xi(x, y) = h(x, y) + b(x, y) = \xi_0 = \text{const.} \tag{14}$$

Expression (14) is the exact solution of systems (1)–(3) and (6)–(8) in the indicated case.

Thus, the regularized SW equations can be treated as an extension of the classical SW equations.

2. NUMERICAL ALGORITHM

Let us construct a finite-difference approximation of the regularized SW equations in a Cartesian coordinate system. Suppose that all the desired variables are defined at grid nodes. The corresponding stencil

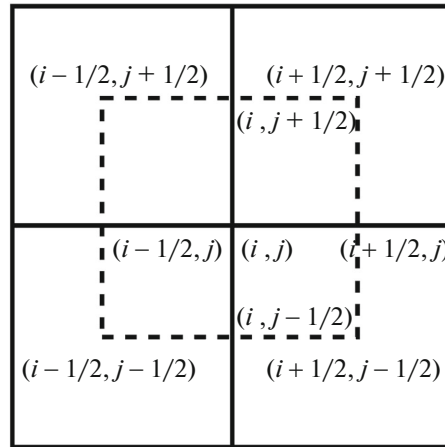


Fig. 1. Stencil for a rectangular spatial grid.

for a rectangular spatial grid is shown in Fig. 1. The variable h will be used to demonstrate computational formulas.

The values of variables at cell centers are defined as the arithmetic mean of their values at neighboring nodes, for example,

$$h_{i+1/2, j+1/2} = 0.25(h_{i,j} + h_{i+1,j} + h_{i,j+1} + h_{i+1,j+1})$$

The values of variables on an edge are calculated as the mean of the values at the points this edge joins:

$$h_{i\pm 1/2, j} = 0.5(h_{i,j} + h_{i\pm 1, j}), \quad h_{i, j\pm 1/2} = 0.5(h_{i,j} + h_{i, j\pm 1}).$$

A similar approximation is used for u_x , u_y and the variable parameter τ . The bottom profile $b(x, y)$ is a given function. Nevertheless, its values at half-integer points have to be determined in the same manner as the values of h and velocity, i.e., by using the above formulas.

To approximate the fluxes j_{mx} and j_{my} , their values are determined at half-integer points on edges. Here and below, for convenience, a superscript is used to denote the x - and y -components. Thus, we need to determine $w_{i+1/2, j}^x$, $w_{i-1/2, j}^x$ and $w_{i, j+1/2}^y$, $w_{i, j-1/2}^y$. The corresponding expressions involve derivatives, which are approximated by central differences. For example, the expressions for $w_{i+1/2, j}^x$ and $w_{i-1/2, j}^x$ are

$$\begin{aligned} w_{i+1/2, j}^x &= \frac{\tau_{i+1/2, j}}{h_{i+1/2, j}} \left(\frac{h_{i+1, j} u_{i+1, j}^x u_{i+1, j}^x - h_{i, j} u_{i, j}^x u_{i, j}^x}{\Delta x} \right. \\ &+ \frac{h_{i+1/2, j+1/2} u_{i+1/2, j+1/2}^x u_{i+1/2, j+1/2}^y - h_{i+1/2, j-1/2} u_{i+1/2, j-1/2}^x u_{i+1/2, j-1/2}^y}{\Delta y} \\ &\left. + \frac{gh_{i+1/2, j}}{\Delta x} (h_{i+1, j} - h_{i, j} + b_{i+1, j} - b_{i, j}) - h_{i+1/2, j} f_{i+1/2, j}^x \right), \\ w_{i-1/2, j}^x &= \frac{\tau_{i-1/2, j}}{h_{i-1/2, j}} \left(\frac{h_{i, j} u_{i, j}^x u_{i, j}^x - h_{i-1, j} u_{i-1, j}^x u_{i-1, j}^x}{\Delta x} \right. \\ &+ \frac{h_{i-1/2, j+1/2} u_{i-1/2, j+1/2}^x u_{i-1/2, j+1/2}^y - h_{i-1/2, j-1/2} u_{i-1/2, j-1/2}^x u_{i-1/2, j-1/2}^y}{\Delta y} \\ &\left. + \frac{gh_{i-1/2, j}}{\Delta x} (h_{i, j} - h_{i-1, j} + b_{i, j} - b_{i-1, j}) - h_{i-1/2, j} f_{i-1/2, j}^x \right). \end{aligned}$$

The values $w_{i, j+1/2}^y$ and $w_{i, j-1/2}^y$ are approximated in a similar fashion.

Using an integro-interpolation method for approximating Eq. (6), we construct an explicit (in time) difference scheme for its solution:

$$\hat{h}_{i,j} = h_{i,j} - \frac{\Delta t}{\Delta x} (j_{i+1/2,j}^x - j_{i-1/2,j}^x) - \frac{\Delta t}{\Delta y} (j_{i,j+1/2}^x - j_{i,j-1/2}^x), \quad (15)$$

where Δt is the time step, Δx and Δy are the mesh sizes in x and y , and $\hat{h}_{i,j}$ is the value of $h_{i,j}$ at the upper time level.

To approximate the tensor Π_{ij} , we use (13) with the expressions involved in w_x^* , w_y^* , and R^* approximated by central differences. All the necessary difference formulas are constructed in a similar manner to the above ones with the use of the stencil shown in Fig. 1. The values of \hat{u}_x and \hat{u}_y at the next time level are calculated using the difference formulas

$$\begin{aligned} \hat{h}\hat{u}_x = & hu_x + \frac{\Delta t}{\Delta x} (\Pi_{i+1/2,j}^{xx} - \Pi_{i-1/2,j}^{xx}) - \frac{\Delta t}{\Delta x} (u_{i+1/2,j}^x j_{i+1/2,j}^x - u_{i-1/2,j}^x j_{i-1/2,j}^x) \\ & - 0.5g \frac{\Delta t}{\Delta x} (h_{i+1/2,j}^2 - h_{i-1/2,j}^2) + \frac{\Delta t}{\Delta y} (\Pi_{i,j+1/2}^{yx} - \Pi_{i,j-1/2}^{yx}) \end{aligned} \quad (16)$$

$$- \frac{\Delta t}{\Delta y} (u_{i,j+1/2}^x j_{i,j+1/2}^y - u_{i,j-1/2}^x j_{i,j-1/2}^y) + \Delta t h_{i,j}^{*(x)} \left(f_{i,j}^x - g \frac{b_{i+1/2,j} - b_{i-1/2,j}}{\Delta x} \right),$$

$$\begin{aligned} \hat{h}\hat{u}_y = & hu_y + \frac{\Delta t}{\Delta x} (\Pi_{i+1/2,j}^{xy} - \Pi_{i-1/2,j}^{xy}) - \frac{\Delta t}{\Delta x} (u_{i+1/2,j}^y j_{i+1/2,j}^x - u_{i-1/2,j}^y j_{i-1/2,j}^x) \\ & + \frac{\Delta t}{\Delta y} (\Pi_{i,j+1/2}^{yy} - \Pi_{i,j-1/2}^{yy}) - \frac{\Delta t}{\Delta y} (u_{i,j+1/2}^y j_{i,j+1/2}^y - u_{i,j-1/2}^y j_{i,j-1/2}^y) \end{aligned} \quad (17)$$

$$- 0.5g \frac{\Delta t}{\Delta y} (h_{i,j+1/2}^2 - h_{i,j-1/2}^2) + \Delta t h_{i,j}^{*(y)} \left(f_{i,j}^y - g \frac{b_{i,j+1/2} - b_{i,j-1/2}}{\Delta y} \right).$$

The expressions for $h_{i,j}^{*(x)}$ and $h_{i,j}^{*(y)}$ are

$$h_{i,j}^{*(x)} = h_{i,j}^x - \tau_{i,j} \left(\frac{h_{i+1/2,j} u_{i+1/2,j}^x - h_{i-1/2,j} u_{i-1/2,j}^x}{\Delta x} + \frac{h_{i,j+1/2} u_{i,j+1/2}^y - h_{i,j-1/2} u_{i,j-1/2}^y}{\Delta y} \right), \quad (18)$$

$$h_{i,j}^{*(y)} = h_{i,j}^y - \tau_{i,j} \left(\frac{h_{i+1/2,j} u_{i+1/2,j}^x - h_{i-1/2,j} u_{i-1/2,j}^x}{\Delta x} + \frac{h_{i,j+1/2} u_{i,j+1/2}^y - h_{i,j-1/2} u_{i,j-1/2}^y}{\Delta y} \right). \quad (19)$$

The regularization parameter is given by the relation

$$\tau = \alpha \frac{\Delta x + \Delta y}{2\sqrt{gh}}, \quad (20)$$

where $0 < \alpha < 1$ is a numerical coefficient chosen to ensure the required stability and accuracy of the algorithm. The characteristic velocity is chosen to be the propagation velocity of long waves: $c = \sqrt{gh}$.

In problems in the SW approximation, the value of the kinematic viscosity ν is, as a rule, very small. Nevertheless, numerical experiments show that, for flows with large Froude numbers, it is convenient to consider the terms Π^{NS} as artificial regularizers and relate ν to τ (see [17]):

$$\nu = \frac{gh^2}{2} \tau.$$

In the computations presented below, we set $\nu = 0$.

The stability condition for the constructed explicit difference scheme is chosen according to the Courant condition imposed on the time step:

$$\Delta t = \beta \left(\frac{\Delta x + \Delta y}{2\sqrt{gh}} \right)_{\min}. \quad (21)$$

In [16] the energy inequality method in the linear approximation was used to obtain a sufficient condition (coinciding with the Courant one) for the stability of a time-explicit difference scheme for solving the regularized equations.

Obviously, due to the use of condition (20), the order of the above difference scheme is reduced and it becomes a first-order accurate scheme. However, the experience gained in the application of similar schemes to gasdynamic and viscous incompressible simulations has shown that they have a number of positive qualities when applied to the computation of unsteady flows with high gradients.

As applied to the SW equations, it was shown in [17] for a number of Riemann problems computed in the framework of the one-dimensional Saint-Venant equations that the numerical method described above is more accurate than the Lax–Friedrichs scheme.

The algorithm presented can naturally be extended to nonuniform spatial grids. Corresponding difference schemes on unstructured triangular meshes were constructed and tested in [18]. In [19] regularized SW equations were derived and corresponding difference schemes for the equations written in a polar coordinate system were constructed.

3. HYDROSTATIC EQUILIBRIUM CONDITION

For many problems, it is necessary that the difference algorithm used satisfy the hydrostatic equilibrium condition. In the English-language literature, such a numerical algorithm is called a *well-balanced scheme* (see, e.g., [20, 21]). This condition means that, in the absence of external forces for a fluid that is initially at rest, the numerical solution must not exhibit spurious perturbations caused by the difference approximation of the bottom irregularities.

To check whether the difference algorithm is well balanced, the equilibrium solution $u_{i,j}^x = u_{i,j}^y = 0$ and $h_{i,j} + b_{i,j} = \text{const}$ is substituted into (15)–(17) to show that the difference equations hold identically for this solution. Indeed, the difference analogues of fluxes (10) and (11) in Eq. (15) vanish in view of relations of the form

$$w_{i-1/2,j}^x = \frac{gh_{i-1/2,j}}{\Delta x} (h_{i,j} - h_{i-1,j} + b_{i,j} - b_{i-1,j}) = 0,$$

$$w_{i,j-1/2}^y = \frac{gh_{i,j-1/2}}{\Delta y} (h_{i,j} - h_{i,j-1} + b_{i,j} - b_{i,j-1}) = 0,$$

which are ensured by the discrete hydrostatic equilibrium conditions in the x and y directions:

$$h_{i,j} + b_{i,j} = h_{i-1,j} + b_{i-1,j} = \text{const}, \quad h_{i,j} + b_{i,j} = h_{i,j-1} + b_{i,j-1} = \text{const}.$$

The difference analogues of the equations of motion (16) and (17) become

$$0 = -g \frac{\Delta t}{\Delta x} (0.5(h_{i+1/2,j}^2 - h_{i-1/2,j}^2) + h_{i,j}^{*(x)}(b_{i+1/2,j} - b_{i-1/2,j})), \quad (22)$$

$$0 = -g \frac{\Delta t}{\Delta y} (0.5(h_{i,j+1/2}^2 - h_{i,j-1/2}^2) + h_{i,j}^{*(y)}(b_{i,j+1/2} - b_{i,j-1/2})). \quad (23)$$

If the difference approximation of $h_{i,j}^x$ and $h_{i,j}^y$ in (18) and (19) is specified in the form of the mean of the values at two neighboring half-integer points in the corresponding x - and y -axes, i.e.,

$$h_{i,j}^x = 0.5(h_{i+1/2,j} + h_{i-1/2,j}), \quad (24)$$

$$h_{i,j}^y = 0.5(h_{i,j+1/2} + h_{i,j-1/2}), \quad (25)$$

then relations (22) and (23) hold identically for equilibrium solution (14) calculated at half-integer points:

$$h_{i+1/2,j} + b_{i+1/2,j} = h_{i-1/2,j} + b_{i-1/2,j}, \quad (26)$$

$$h_{i,j+1/2} + b_{i,j+1/2} = h_{i,j-1/2} + b_{i,j-1/2}. \quad (27)$$

Thus, the difference scheme constructed above is well balanced. This property is important for the numerical simulation of slow flows, which must not be affected by spurious perturbations caused by the differ-

ence approximation of bottom irregularities. In the case of highly unsteady intensive flows, when such perturbations are not essential, it is sufficient to use the simpler approximation

$$h_{i,j}^x = h_{i,j}^y = h_{i,j}. \tag{28}$$

The construction of well-balanced difference schemes for high-order accurate algorithms faces substantial difficulties (see, e.g., [21]). For the algorithm proposed, this property holds, since the adaptive τ -dissipation involved vanishes for stationary equilibrium solutions. In [22] new versions of conservative spatial discretizations that satisfy the energy conservation laws and are well balanced were constructed for the barotropic quasi-gasdynamic equations with external forces. A special case of these discretizations is the difference scheme described above.

In [4, 5] a well-balanced algorithm for solving the SW equations for one-dimensional plane flows was presented and formula (24) was derived for the first time in the one-dimensional case. In [18] formulas (24) and (25) for $h_{i,j}^{*(x)}$ and $h_{i,j}^{*(y)}$ were extended to the approximation of the regularized SW equations on unstructured meshes. In [19] it was shown for a rotating flow that the accuracy of an unbalanced difference scheme for an equilibrium solution is $\sim 10^{-3}$, while, in the case of a well-balanced scheme, the accuracy increases up to $\sim 10^{-13} - 10^{-14}$. These computations were performed in a polar coordinate system.

4. MOVING SHORELINE

In many applications associated, for example, with the numerical simulation of river flooding and tsunami runup, the boundaries of dry-bed areas have to be determined. In these zones, the water height is considered to be zero: $h(x, y) = 0$. Various approaches are used to describe dry-bed areas in numerical algorithms intended for the SW equations (see, for example, [21, 23, 24]). In our algorithm based on the regularized SW equations, we apply a widely used method described, for example, in [23].

According to this approach, the water in a dry-bed area is assumed to be at rest. Then the water depth is computed using the condition that, for small $h_{i,j}$, the flow velocity is zero ($u_{i,j} = 0$), i.e.,

$$\begin{aligned} \hat{u}_{i,j} &= h_{i,j} u_{i,j} / \hat{h}_{i,j}, & h_{i,j} > \varepsilon_{i,j}, \\ \hat{u}_{i,j} &= 0, & h_{i,j} < \varepsilon_{i,j}, \end{aligned} \tag{29}$$

where $\varepsilon_{i,j}$ is a cutoff parameter, which depends on the problem under consideration.

In contrast to [23], the numerical algorithm based on the regularized SW equations involves parameter τ , which is contained in all regularizing terms. For small h , a similar constraint is imposed on τ :

$$\begin{aligned} \tau_{i,j} &= \alpha \frac{\Delta x + \Delta y}{2\sqrt{gh_{i,j}}}, & h_{i,j} > \varepsilon_{i,j}, \\ \tau_{i,j} &= 0, & h_{i,j} < \varepsilon_{i,j}. \end{aligned} \tag{30}$$

If $b(x, y) \neq \text{const}$ and the gradient of $b(x, y)$ is bounded, it is convenient to relate ε to the bottom slope by the inequality

$$\varepsilon > \Delta x \left| \frac{\partial b}{\partial x} \right|, \tag{31}$$

i.e., the cutoff parameter is a variable depending on the bottom topography and the chosen spatial grid. In the case of rectangular or unstructured meshes, the difference analogue of condition (31) can be represented as

$$\varepsilon_{i,j} > \max_{(m,k) \in \text{stencil}} (b_{m,k} - b_{i,j}).$$

Specifically, for a two-dimensional rectangular grid, this condition can be conveniently written as

$$\varepsilon_{i,j} = \varepsilon_0 \max((b_{i+1,j} - b_{i,j}), (b_{i-1,j} - b_{i,j}), (b_{i,j+1} - b_{i,j}), (b_{i,j-1} - b_{i,j})), \tag{32}$$

where ε_0 is a tuning parameter.

5. PROBLEM OF DAM BREAK IN A DRY-BED ZONE

We consider a one-dimensional Riemann problem modeling the flow associated with a dam break wave propagating in a dry-bed area, where $h = 0$. Let the size of the domain be $[0, 50]$ m. A discontinuity

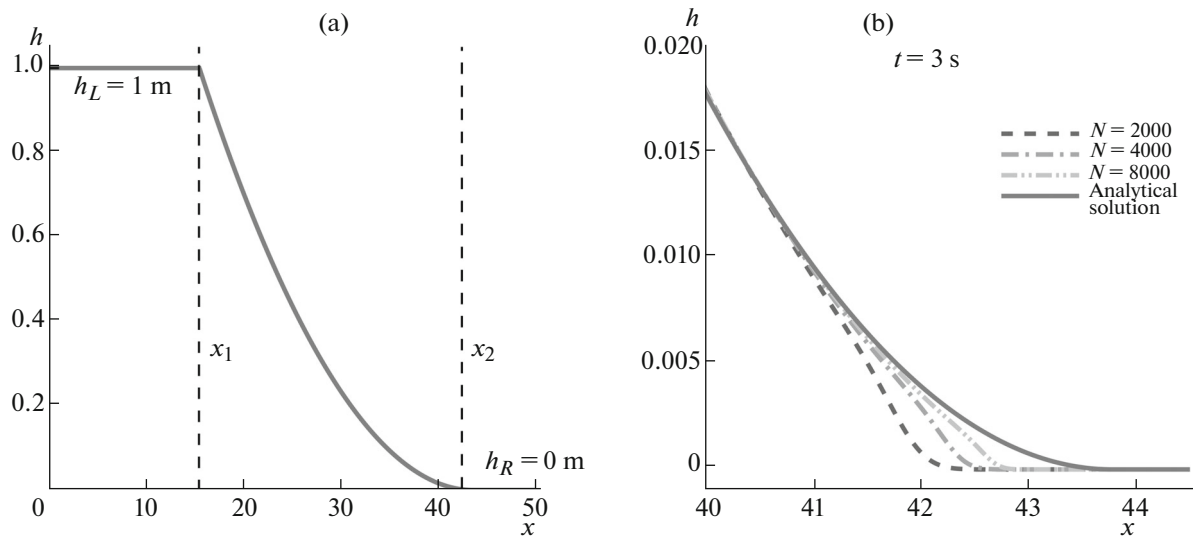


Fig. 2. Water height h in the Riemann problem: (a) self-similar solution and (b) convergence as the grid is refined on the interval $[40, 44.5]$ at the time $t = 3$ s for $\varepsilon = 0.0001$, $\alpha = 0.2$, and $\beta = 0.1$.

is placed at the center of the domain at the point with coordinate $x = 25$ m. At the initial time the fluid is at rest and the velocities to the left and right of the discontinuity are zero ($u_L = 0$ m/s, $u_R = 0$ m/s). In the left domain, the water height is $h_L = 1.0$ m, and there is a dry bed ($h_R = 0$ m) on the right.

On the basis of the general solution to the Riemann problem [25, 26], the analytical solution of the given Riemann problem is written as

$$h(x), u(x) = \begin{cases} h = h_L, & u = 0, & x < x_1 = -t\sqrt{gh_L}, \\ h = \frac{1}{9g} \left(2\sqrt{gh_L} - \frac{x}{t} \right)^2, & u = \frac{2}{3} \left(\sqrt{gh_L} + \frac{x}{t} \right), & x_1 < x < x_2 = 2t\sqrt{gh_L}, \\ h = h_R, & u = 0, & x_2 < x. \end{cases}$$

This solution is used to determine the velocity of the moving shoreline $x_2 = 2t\sqrt{gh_L}$. Note that the exact location of the moving shoreline cannot be determined in the numerical computation, since the domain with $h < \varepsilon$ is eliminated from the consideration due to the dry bed condition.

The computations were conducted up to the time $t = 5$ s on four refined meshes with $\Delta x = 0.05$ m ($N = 1000$), $\Delta x = 0.025$ m ($N = 2000$), $\Delta x = 0.0125$ m ($N = 4000$), and $\Delta x = 0.00625$ m ($N = 8000$); here, N is the number of points in space. The other computational parameters were specified as follows: the regularization parameter $\alpha = 0.2$, the Courant number $\beta = 0.1$, and the cutoff parameter $\varepsilon = 0.0001$ m. When ε was increased to 0.001 m, the numerical results near the moving shoreline became less accurate. When ε was decreased 0.00001 m, the time step had to be reduced to ensure stable computations and, accordingly, β was reduced to 0.01. The poorer stability of the algorithm was caused by the sharp increase in the Froude number $Fr = u/\sqrt{gh}$ near the dry-bed areas.

The general form of the solution and the convergence of the numerical solution to the analytical one are presented in Fig. 2. Specifically, Fig. 2a shows the self-similar solution, while Fig. 2b illustrates the convergence as the grid is refined on the interval $[40, 44.5]$ at the time $t = 3$ s for $\varepsilon = 0.0001$, $\alpha = 0.2$, and $\beta = 0.1$. It can be seen that the numerical and analytical solutions agree on nearly the entire plot, and a noticeable difference occurs only on the moving shoreline. The plots show that the accuracy of the numerical solution is improved with decreasing mesh size. The influence of α on the accuracy of the determined shoreline is insignificant.

The position of the shoreline is affected by the value of ε . Due to the numerical errors, ε cannot be zero. When ε is zero, any numerical perturbation for problems with dry areas $h = 0$ leads to negative values of h . From a physical point of view, for example, in the case of a flow 10 m deep, we neglect the motion

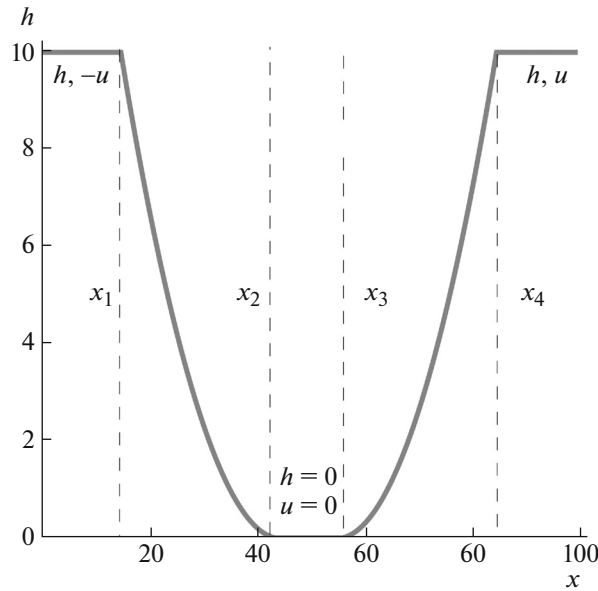


Fig. 3. Self-similar solution in the diverging fluid problem. The dry bed is formed over the domain $[x_2, x_3]$. The points x_2 and x_3 move in opposite directions.

of the fluid in a layer of thickness 10 cm ($\epsilon = 0.1$ m) or 1 cm ($\epsilon = 0.01$ m), respectively. The parameter ϵ has to be chosen according depending on the problem under consideration. For example, when the runoff of a 10-meter wave is modeled, the motion of the fluid in a 1-cm thick layer near the dry bed can be neglected.

In the one-dimensional Riemann problem with a dry bed, the fluid runs over a dry area. A more complicated problem is one in which the fluid runs down a surface to form a dry area. Such a problem is addressed in the next section.

6. RIEMANN PROBLEM WITH A DIVERGING FLUID

Consider a Riemann problem with a fluid moving in opposite directions (see [22]). Given the domain $[0, 100]$ m, a discontinuity is placed at the center $x = 50$ m of the interval. At the initial time the water height is everywhere constant ($h_L = h_R = 10$ m), but the velocities are opposite ($u_R = -u_L = 15$ m/s). The self-similar solution of this problem is schematically shown in Fig. 3. Here, the points x_2 and x_3 move in opposite directions.

A dry bed appears in the domain $[x_2, x_3]$ only if $u_R > 2\sqrt{gh_R}$. Note that the velocity u has jump discontinuities at the points x_2 and x_3 . The analytical solution consists of two rarefaction waves and a dry-bed area. The rarefaction wave on the interval $[x_1, x_2]$ is described by the self-similar solution (see [25, 26])

$$\frac{3}{2}u = c_1 + \frac{x}{t}, \quad 3\sqrt{gh} = 2c_1 - \frac{x}{t}.$$

Similarly, the solution in the domain $[x_3, x_4]$ is described by the functions

$$\frac{3}{2}u = c_2 + \frac{x}{t}, \quad 3\sqrt{gh} = \frac{x}{t} - 2c_2.$$

The constants c_1 and c_2 are found using the initial conditions:

$$c_1 = -\frac{u_R}{2} + \sqrt{gh_R}, \quad c_2 = \frac{u_R}{2} - \sqrt{gh_R}.$$

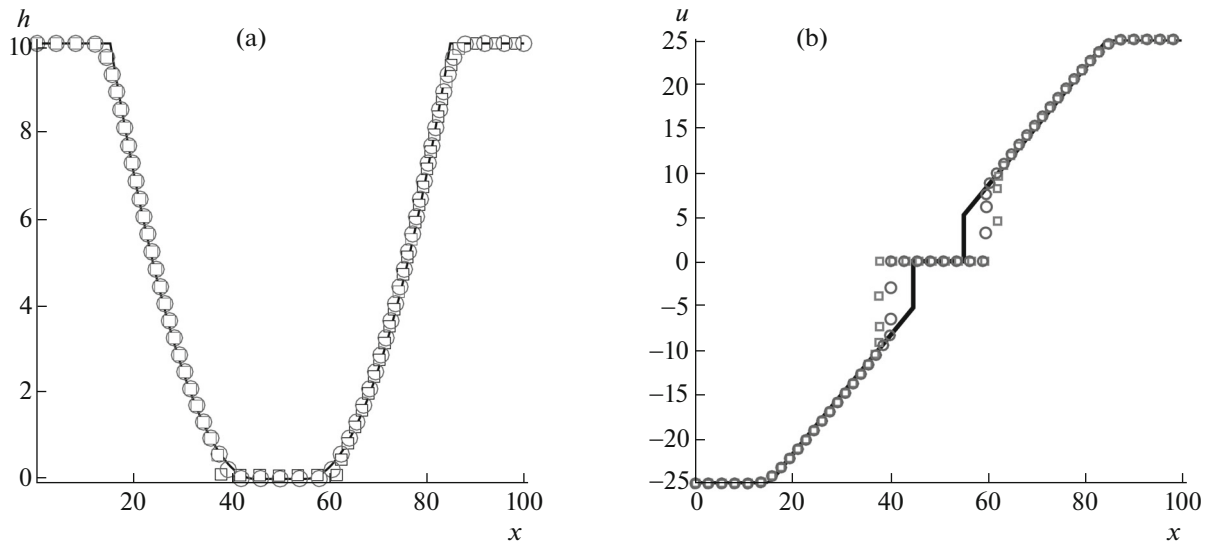


Fig. 4. (a) Water height and (b) velocity at the time $t = 1$ s. The exact solution is depicted by the solid curve. The numerical solutions for $\varepsilon = 10$ cm and $\varepsilon = 1$ cm are shown by squares and circles, respectively.

The analytical solution of the problem is given by

$$h(x), u(x) = \begin{cases} h = h_R, & u = -u_R, & x < x_1 = -t(u_R + \sqrt{gh_R}), \\ h = \frac{1}{9g} \left(2c_1 - \frac{x}{t}\right)^2, & u = \frac{2}{3} \left(c_1 + \frac{x}{t}\right), & x_1 < x < x_2 = -t(u_R - 2\sqrt{gh_R}), \\ h = 0, & u = 0, & x_2 < x < x_3 = t(u_R - 2\sqrt{gh_R}), \\ h = \frac{1}{9g} \left(2c_2 - \frac{x}{t}\right)^2, & u = \frac{2}{3} \left(c_2 + \frac{x}{t}\right), & x_3 < x < x_4 = t(u_R + \sqrt{gh_R}), \\ h = h_R, & u = u_R, & x_4 < x. \end{cases}$$

The problem was computed up to the time $t = 2$ s. The parameters were specified as $\alpha = 0.5$, $\beta = 0.01$, and $\Delta x = 0.025$ m ($N = 2000$). The computations were performed for two cutoff parameters, $\varepsilon = 0.1$ m and $\varepsilon = 0.01$ m, to show the influence of ε on the numerical results.

Figure 4a shows the water height distribution at $t = 1$ s. The analytical solution is depicted by the solid line. The numerical solutions for $\varepsilon = 10$ cm and $\varepsilon = 1$ cm are shown by squares and circles, respectively. It can be seen that the numerical and analytical solutions agree well on nearly the entire plot. Figure 4b presents the velocity distribution at the time $t = 1$ s. It can be seen that the position of the shoreline is more accurate when ε is smaller.

7. PERIODIC WAVE OVER A CONSTANT-SLOPE BOTTOM: COMPARISON OF THE NUMERICAL AND EXACT SOLUTIONS

This problem was used as a test one, for example, in [27], where the numerical solution was compared with the exact solution, namely, with the Carrier–Greenspan periodic wave [28]. This solution is applied as a benchmark to verify the ability of a numerical algorithm to simulate wave runup and rundown over a sloping beach. Specifically, it allows one to verify the shoreline boundary condition.

According to [29], it is convenient to write the analytical solution of this problem in the dimensionless variables

$$\begin{aligned} \tilde{x} &= x/L, & \tilde{u} &= u/\sqrt{g \tan \gamma L}, \\ \tilde{\xi} &= \xi/\tan \gamma L, & \tilde{t} &= t/\sqrt{L/(g \tan \gamma)}. \end{aligned}$$

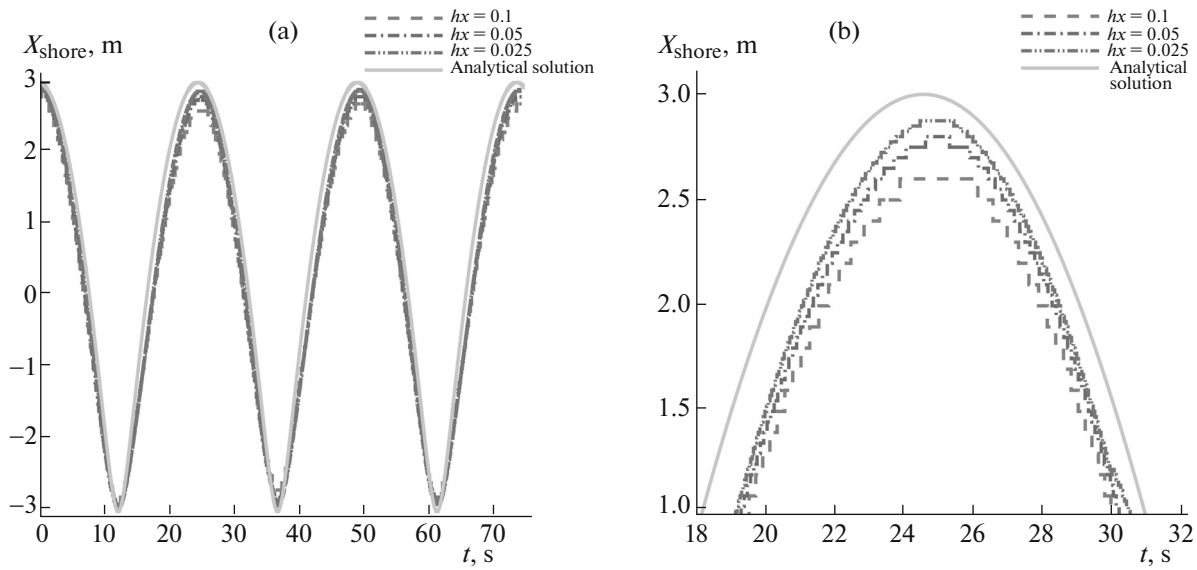


Fig. 5. (a) Coordinate of the shoreline as a function of time for three mesh sizes: $\Delta x = 0.1$ m, $\Delta x = 0.05$ m, and $\Delta x = 0.025$ m and (b) a fragment.

The solution is written in implicit form as

$$\begin{aligned} \tilde{u} &= -A \frac{J_1(\tilde{\sigma})}{\tilde{\sigma}} \sin(\tilde{\lambda}), & \xi &= \frac{A}{4} J_0(\tilde{\sigma}) \cos(\tilde{\lambda}) - \frac{\tilde{u}^2}{4}, \\ \tilde{x} &= \xi - \frac{\tilde{\sigma}^2}{16}, & \tilde{t} &= \frac{\tilde{\lambda}}{2} - \tilde{u}. \end{aligned}$$

The form of the solution suggests that the fluid is at rest at the time $t = 0$. Then there appears periodic motion; its period is $T = \pi\sqrt{L/(g \tan \gamma)}$. Here, $c = \sqrt{gh}$ is the dimensionless analogue of the long-wave velocity $c = \sqrt{gh}$. Therefore, the substitution of A yields the coordinate x and the velocity u at the moving shoreline. For the indicated expression to be valid, it is necessary that A be bounded: $0 \leq A \leq 1$.

The problem considered below corresponds to the following case: $A = 0.6$, $g = 9.8$ m/s², the length of the domain is $L = 20$ m, and the slope angle is $\tan \gamma = 1/30$. The computational domain is the interval $[-100$ m, 10 m]. The bottom has a constant slope: $b(x) = \tan \gamma x$. The solution at $t = 0$ is used as initial conditions. On the left boundary of the domain, we set time-periodic boundary conditions for h and u obtained from the exact solution at $x_0 = -100$ m.

The computations were performed for three mesh sizes: $\Delta x = 0.1$ m, $\Delta x = 0.05$ m, and $\Delta x = 0.025$ m. The parameters of the numerical algorithm were specified as $\alpha = 0.2$ and $\beta = 0.1$ for all mesh sizes. The cutoff parameter was chosen according to (31). Since the bottom had a constant slope, three different values of $\varepsilon = \Delta x \tan \gamma$ were chosen for three different steps, namely, $\varepsilon = 1/300$ m, $\varepsilon = 1/600$ m, and $\varepsilon = 1/1200$ m.

In Fig. 5, the coordinate of the moving shoreline, which separates the inundated and dry areas, is plotted as a function of time over three periods $3T$. The period is $T = \pi\sqrt{L/(g \tan \gamma)}$. The exact solution is depicted by the solid line, while the numerical solutions for $\Delta x = 0.1$ m, $\Delta x = 0.05$ m, and $\Delta x = 0.025$ m are shown by dashed curves. In the plot, the mesh size Δx is denoted by hx .

Variations in the mesh size lead to variations in $\varepsilon = \Delta x \tan \gamma$, but have a small effect on the position of the moving shoreline. The variations associated with a decrease in the mesh size are noticeable only near the peak values (see Fig. 5a). As the mesh size decreases, the numerical results approach the analytical solution (see Fig. 5b).

Figure 6 shows the distribution of the velocity u at $t = 5$ s. It can be seen that the velocity has a discontinuity near the moving shoreline. The analytical and numerical solutions are presented for three mesh sizes: $\Delta x = 0.1$, 0.05 , and 0.025 m. The other parameters of the numerical algorithm are the same as in

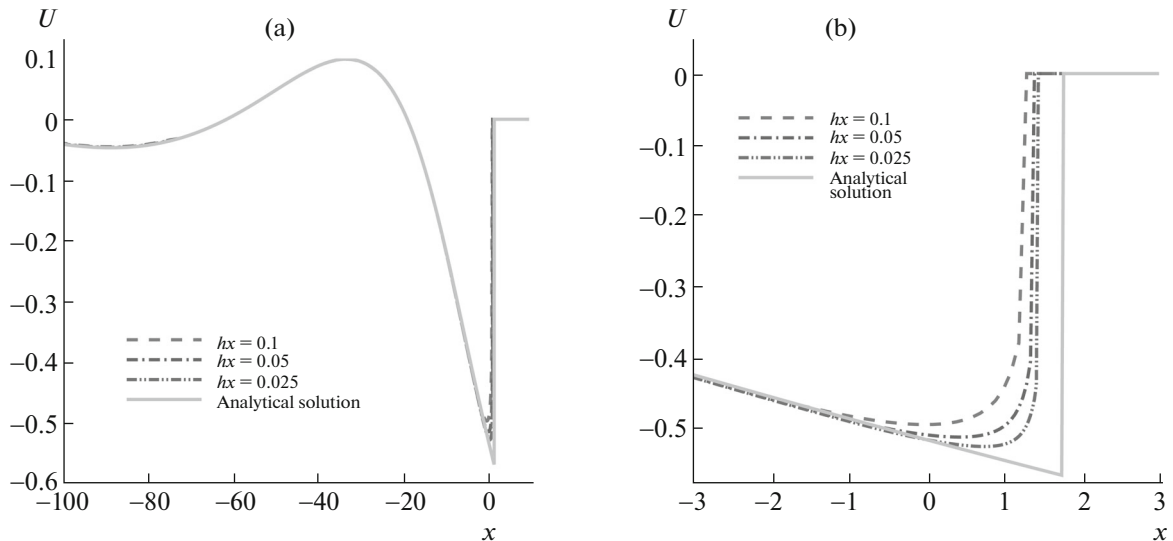


Fig. 6. (a) Velocity distribution u at the time $t = 5$ s for three mesh sizes: $\Delta x = 0.1$ m, $\Delta x = 0.05$ m, and $\Delta x = 0.025$ m and (b) a fragment.

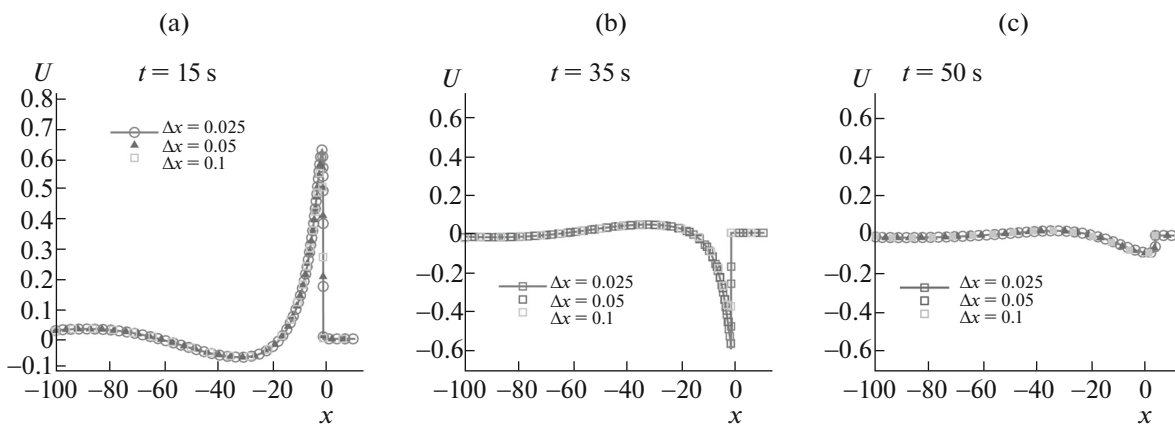


Fig. 7. Velocity distribution u at the times (a) $t = 15$ s, (b) $t = 35$ s, and (c) $t = 50$ s.

the preceding example: $\alpha = 0.2$ and $\beta = 0.1$. Figure 6a displays the velocity distribution over the entire interval $[-100$ m, 10 m], while Fig. 6b shows its fragment near the moving shoreline. The differences between the numerical and exact solutions are noticeable only near the shoreline.

Figures 7 and 8 show the numerical results for u and $\xi = h + b$ at three consecutive times: $t = 15$, 35 , and 50 s. It can be seen that the jump in velocity is smoothed out, but the numerical solution approaches the analytical one with a decrease in Δx and a corresponding decrease in ϵ for all times.

8. NUMERICAL SIMULATION OF TSUNAMI WAVES

The numerical simulation of runup onto a beach for waves of various types, including tsunamis, is an important fluid dynamics problem. In a number of cases, it can be solved on the basis of the SW equations [3]. The numerical results for two test problems presented in this section suggest that a promising approach is based on regularized SW equations with boundary conditions added to describe moving dry-bed areas. A characteristic feature of these problems is that the entire domain, waves, and wave–shore interaction zones (where a dry bed is formed) have substantially different scales.

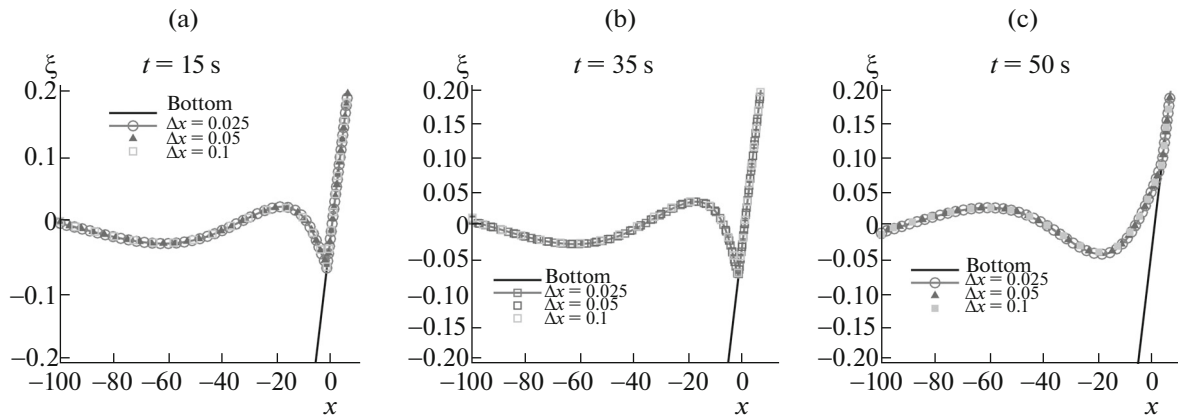


Fig. 8. Profiles of the free surface elevation ξ at the times (a) $t = 15$ s, (b) $t = 35$, and (c) $t = 50$ s.

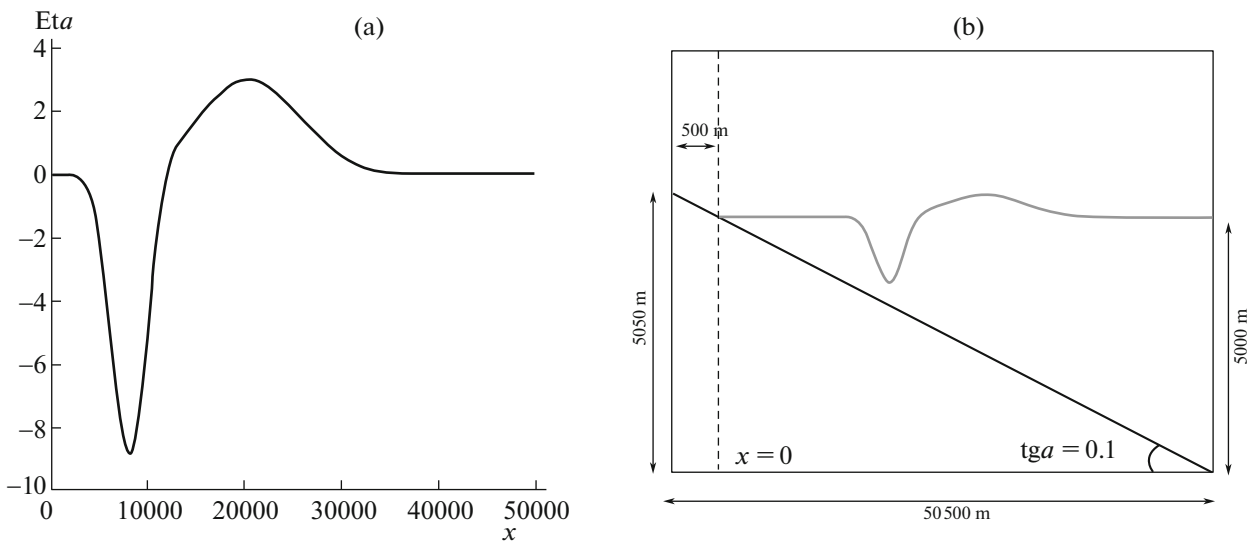


Fig. 9. Initial perturbation of ξ and (a) a fragment.

8.1. Tsunami Runup onto a Constant-Slope Beach

The formulation of the problem and analytical results to be used as a benchmark can be found in [30]. Specifically, these are data on the initial fluid distribution; analytical distributions of ξ and u at three times $t_1 = 160$ s, $t_2 = 175$ s, and $t_3 = 220$ s; and information on the shoreline motion over the time interval $[0, 355]$ s.

The fluid distribution at $t = 0$ is presented in Fig. 9, which shows the free surface elevation $\xi = h + b$ and a sloping beach whose profile b has a constant slope angle γ ($\tan \gamma = 0.1$). Figure 9a shows the perturbation of the free surface elevation vs. coordinate. The computational domain is the interval $[-500, 50000]$ m. At the initial time $t = 0$, the water is at rest and a perturbation of the free surface elevation is specified as the water height distribution on the interval $[0, 50000]$ m. The domain $[-500, 0]$ is occupied by a dry bed, where $h = 0$. The dry bed conditions are set on the left, and a constant water height $h(x = 50000 \text{ m}) = 5000$ m is held on the right.

Note that the horizontal and vertical scales are widely different. The fluid occupies a domain of 50 km, while the difference between the maximum and minimum free surface elevations is 10 m, as can be seen from in the figure. The shape of the free fluid surface is schematically shown in Fig. 9a.

The computations were performed on refined meshes with steps $\Delta x = 5, 2,$ and 1 m. According to the condition $\epsilon = \Delta x \tan \gamma$, three different mesh sizes corresponded to different values of ϵ . To demonstrate the influence of the regularization parameter, we used two values, $\alpha = 0.3$ and $\alpha = 0.4$. The Courant

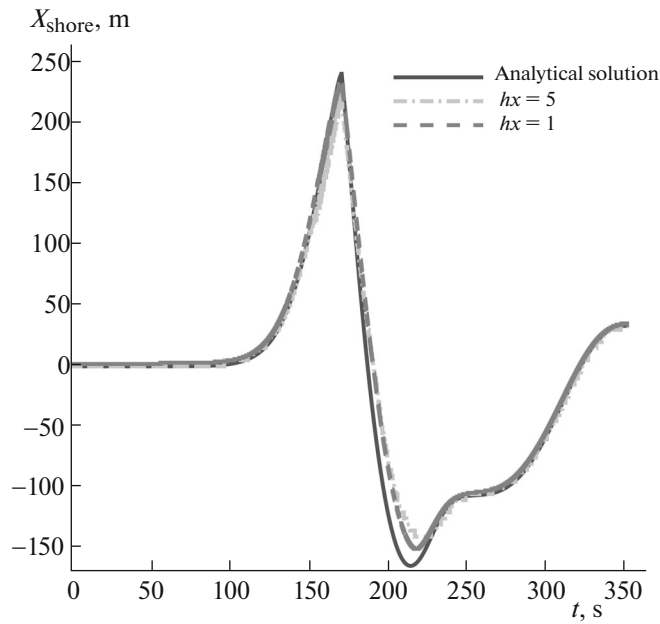


Fig. 10. Shoreline coordinate as a function of time. The exact solution is depicted by the solid curve. The numerical solutions obtained on grids with $\Delta x = 5$ m and $\Delta x = 1$ m are shown by dash-dotted and dashed curves, respectively.

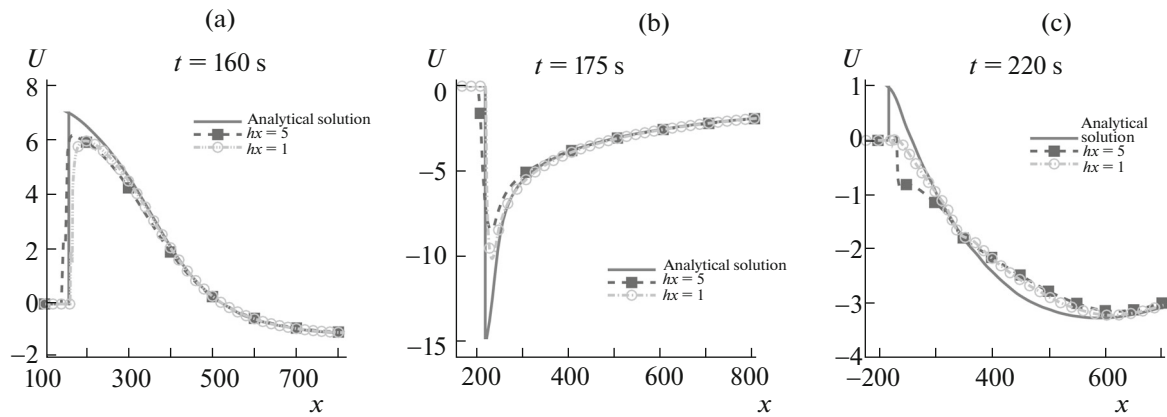


Fig. 11. Velocity profiles u at the times $t = 160, 175,$ and 220 s.

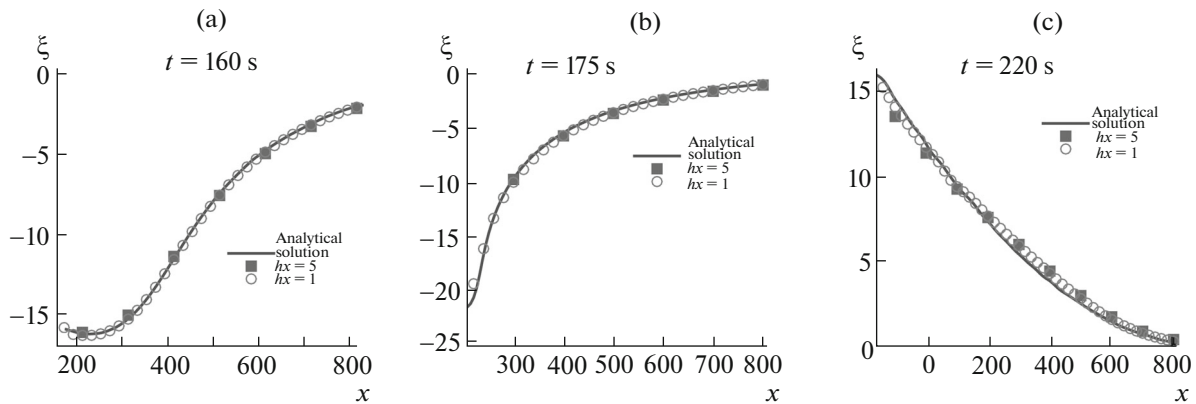


Fig. 12. Perturbation of the free fluid surface ξ at the times $t = 160, 175,$ and 220 s.

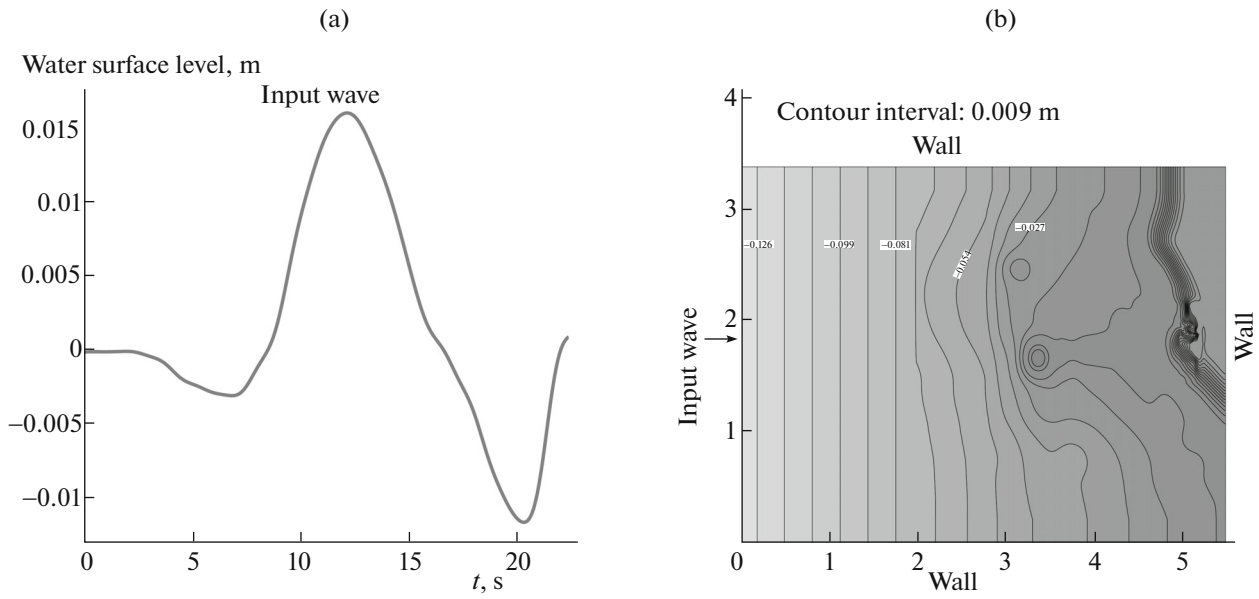


Fig. 13. (a) Water surface level in the input wave and (b) the bottom topography in the Monai Valley experiment.

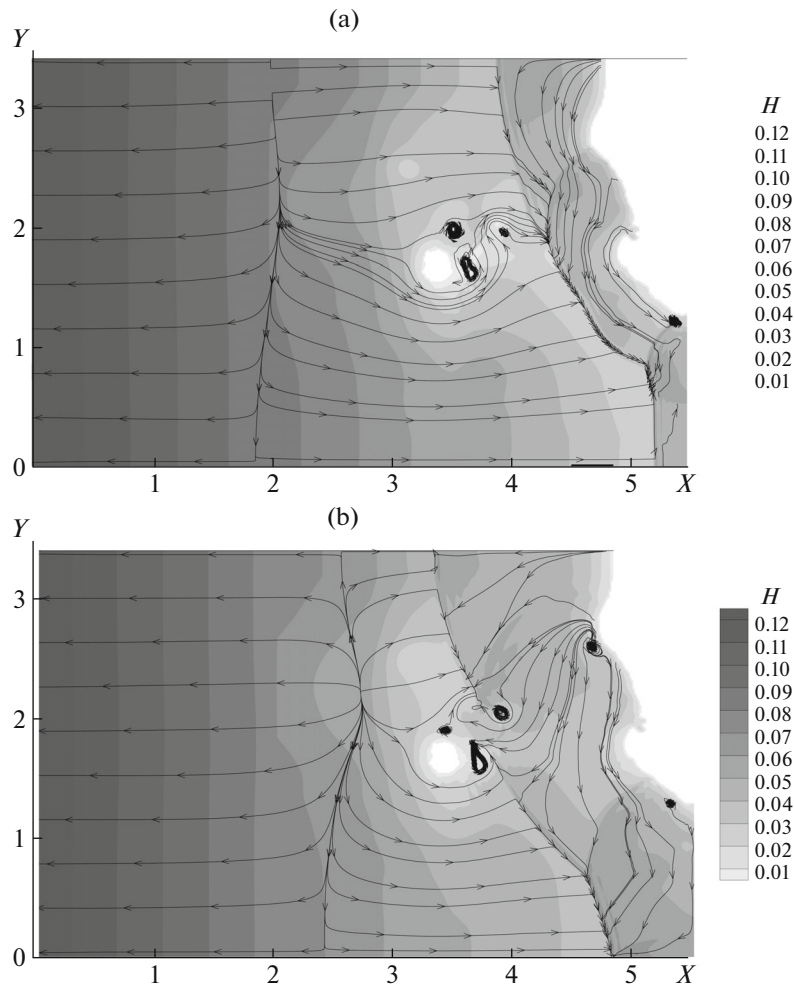


Fig. 14. Contour lines of h and streamlines at the times $t = 17$ and 18 s.

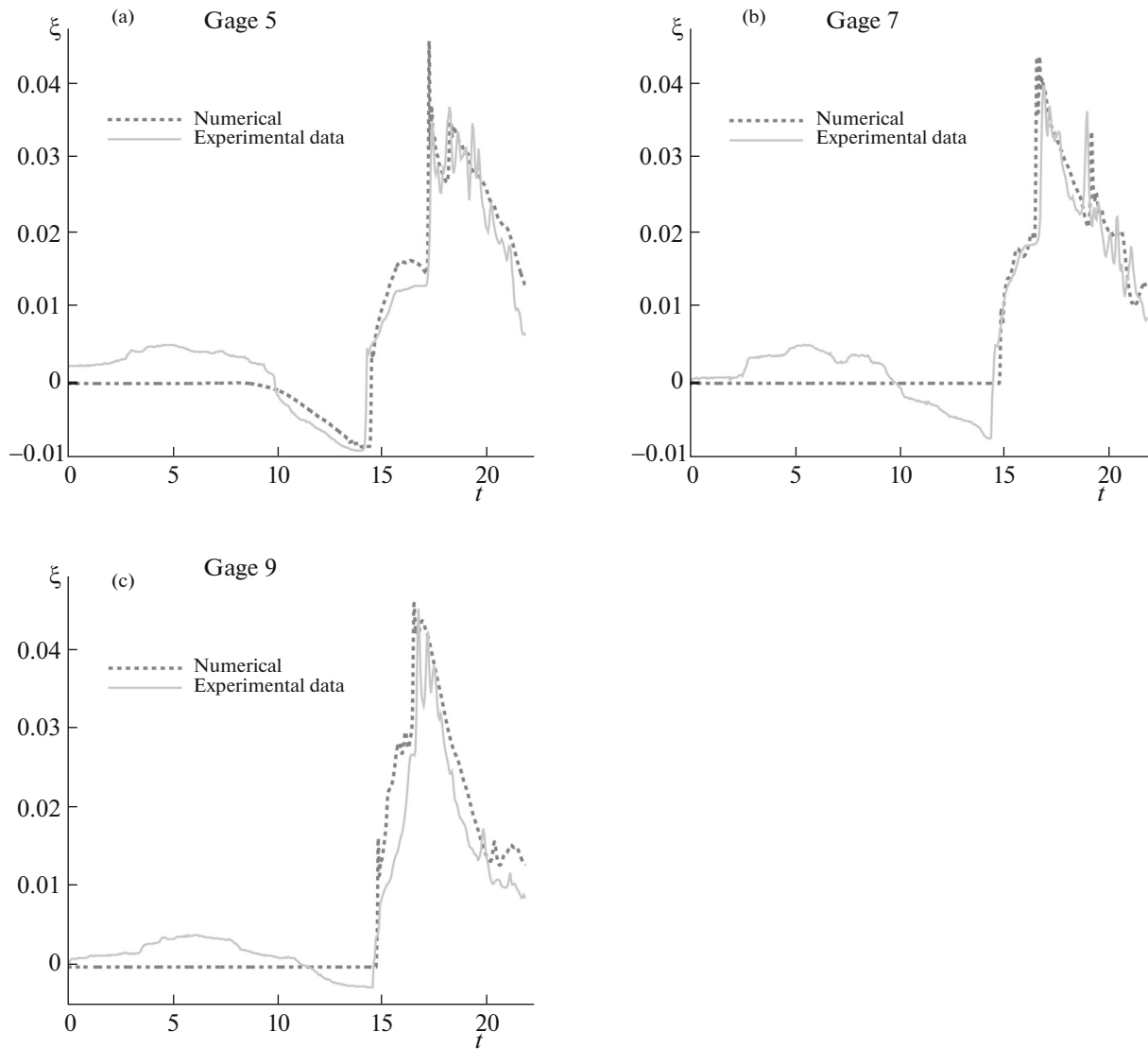


Fig. 15. Comparison of the experimental surface elevations ξ measured at gages 5, 7, and 9 with numerical results: experiment (solid) and numerical simulation (broken).

number was specified as $\beta = 0.5$. It was found that $\alpha = 0.3$ is the optimal value for the given problem. The plots presented below correspond to $\alpha = 0.4$ and $\Delta x = 5$ and 1 m and compare the exact and numerical solutions.

Figure 10 shows the shoreline coordinate for two mesh sizes as compared with the exact solution. The exact solution is depicted by the solid curve. The numerical results for $\Delta x = 5$ and 1 m are shown by broken curves.

Figure 11 compares the numerical results and the exact solution for the velocity distribution at three times $t = 160, 175,$ and 220 s. In the plots of u , noticeable differences between the numerical and exact velocities are observed in the jump zone adjacent to the shoreline. A similar effect takes place in an earlier considered problem (see Fig. 7).

Figure 12 compares the numerical results and the exact solution for $\xi = h + b$ at the same three times $t = 160, 175,$ and 220 s. On the presented scale, no differences can be seen between the exact and numerical solutions on both grids.

The above figures suggest that the solution converges as the spatial grid is refined.

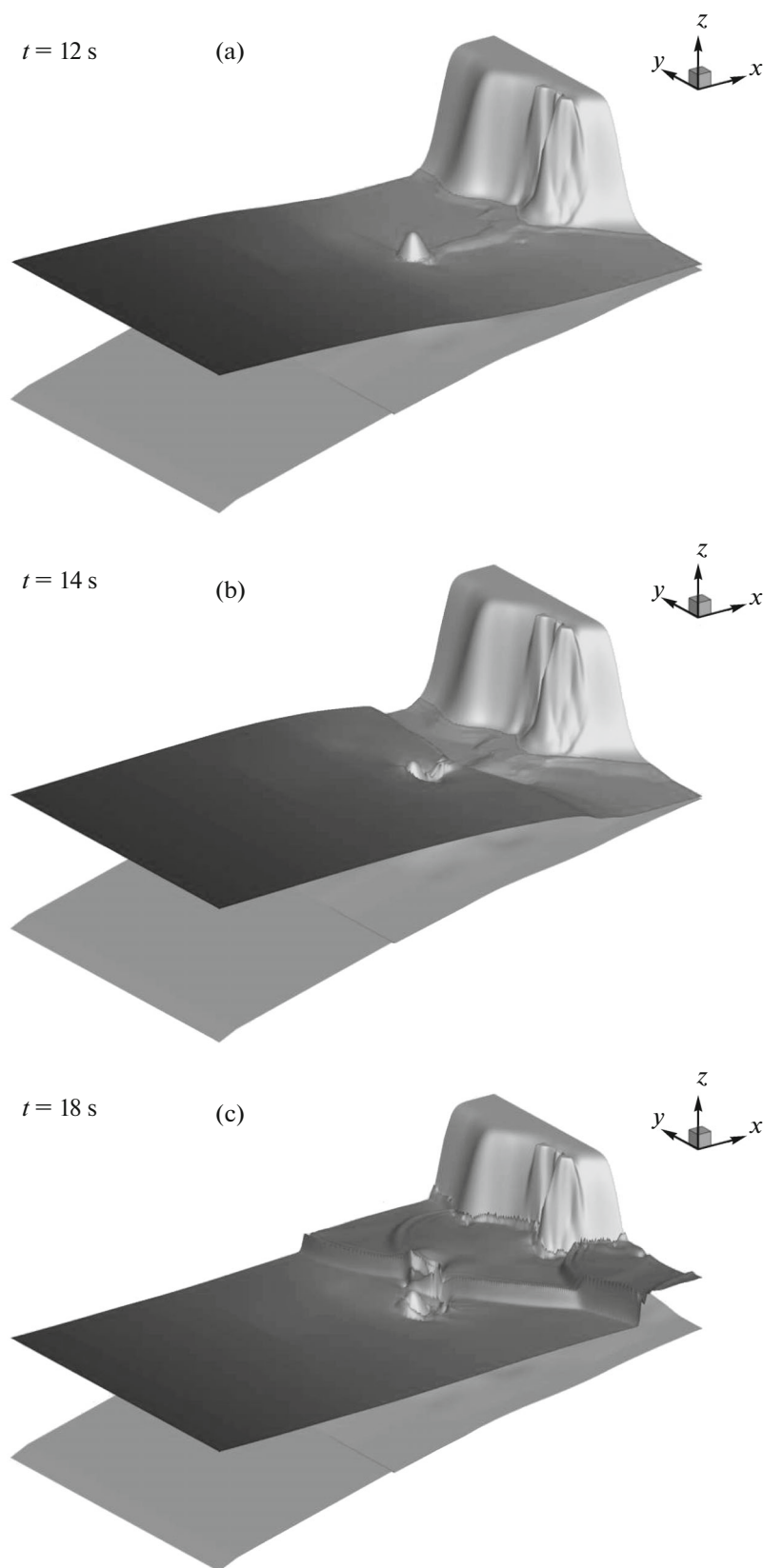


Fig. 16. Three-dimensional fluid profile $\xi(x, y)$ and the bottom topography $b(x, y)$. Wave runup at the times $t = 12, 14,$ and 18 s.

8.2. Tsunami Runup onto Beach of Complex Geometry

The problem of tsunami runup onto a beach of complex geometry is used to test the capabilities and features of various numerical algorithms. Numerical results are compared with results of a laboratory experiment. A 1 : 400 laboratory model based on actual bathymetry was constructed in the experiment. The goal was to simulate the Okushiri tsunami, which occurred in Monai Valley in 1993. Its characteristic feature was an extremely high runup of 31.7 m. The experiment was performed at Central Research Institute for Electric Power Industry in Abiko, Japan. The bathymetry data, initial and boundary conditions, and experimental results can be found in [31].

A similar problem was considered in [22, 32]. In practical applications, it is important that numerical results can be compared with laboratory experiments.

In the given problem, the computational domain is a rectangle 5.448 m long and 3.402 m wide. All the sides of the domain, except for the left boundary, are solid walls. The level h on the left boundary is set by the input wave (Fig. 13a). The bottom topography is shown in Fig. 13b, where the contour interval is 0.009 m. The maximum slope of the beach is not high ($\tan\gamma \sim 0.1$), which makes it possible to use the SW approximation.

The original bathymetry data were presented on a grid with a step of 0.014 m. This step was used for computations on a rectangular grid with $\Delta x = \Delta y$. The numerical parameters were specified as $\alpha = 0.1$ and $\beta = 0.1$. The computations were conducted up to the time $t = 22$ s. The cutoff parameter was specified according to (32) with the coefficient $\varepsilon_0 = 3$.

The streamlines show a complex unsteady flow pattern. This can be seen in Fig. 14, which presents the distribution of h together with streamlines at the times $t = 17$ and 18 s. The dry bed areas are shown in white.

The numerical results were compared with experimental measurements of surface elevations made at three gages numbered by digits 5, 7, and 9 (gage 5: $(x, y) = (4.521, 1.196)$, gage 7: $(x, y) = (4.521, 1.696)$, and gage 9: $(x, y) = (4.521, 2.196)$). The numerical and experimental results are compared in Fig. 15. The plots reveal that they are in good agreement. Note the coincidence of the peak values. The coincidence of the maximum locations in time means that wave propagation and fluid disturbances are adequately described by the model. The difference between the numerical and experimental results on short time intervals can be eliminated by decreasing the cutoff parameter ε .

For illustrative purposes, Fig. 16 shows the three-dimensional water height distributions at three characteristic times: $t = 12, 14$, and 18 s.

CONCLUSIONS

It was shown that the regularized shallow water equations and a numerical algorithm based on them and supplemented with the well-balanced property and conditions ensuring the formation of dry-bed areas provide a convenient and reliable tool for the numerical simulation of flows associated with wave motion in nearshore zones.

ACKNOWLEDGMENTS

This work was supported by the Russian Foundation for Basic Research, project no. 13-01-00703-a.

REFERENCES

1. J. J. Stoker, *Water Waves* (Wiley, New York, 1957; Inostrannaya Literatura, Moscow, 1959).
2. A. G. Kulikovskii, N. V. Pogorelov, and A. Yu. Semenov, *Mathematical Aspects of Numerical Solution of Hyperbolic Systems* (Fizmatlit, Moscow, 2001; Chapman and Hall/CRC, London, 2001).
3. B. W. Levin and M. A. Nosov, *Physics of Tsunamis* (Springer, Berlin, 2008).
4. T. G. Elizarova and O. V. Bulatov, "Regularized shallow water equations and a new method of simulation of the open channel flows," *Int. J. Comput. Fluids*, **46**, 206–211 (2011).
5. O. V. Bulatov and T. G. Elizarova, "Regularized shallow water equations and an efficient method for numerical simulation of shallow water flows," *Comput. Math. Math. Phys.* **51** (1), 160–173 (2011).
6. T. G. Elizarova, *Quasi-Gas Dynamic Equations* (Nauchnyi Mir, Moscow, 2007; Springer-Verlag, Berlin, 2009).
7. Yu. V. Sheretov, *Continuum Dynamics under Spatiotemporal Averaging* (NITs Regul'yarnaya i Khaoticheskaya Dinamika, Moscow, 2009).

8. T. G. Elizarova, A. A. Zlotnik, and O. V. Nikitina, Preprint Nos. 33, 36, IPM RAN (Keldysh Institute of Applied Mathematics, Russian Academy of Sciences, Moscow, 2011).
9. T. G. Elizarova, M. A. Istomina, and N. K. Shelkovnikov, “Numerical simulation of solitary wave generation in a wind-water circular tunnel,” *Math. Models Comput. Simul.* **4** (6), 552–559 (2012).
10. O. V. Bulatov, “Analytical and numerical Riemann solutions of the Saint Venant equations for forward- and backward-facing step flows,” *Comput. Math. Math. Phys.* **54** (1), 158–171 (2014).
11. T. G. Elizarova and D. A. Saburin, “Numerical modeling of liquid fluctuations in fuel tanks,” *Math. Models Comput. Simul.* **5** (5), 470–478 (2013).
12. T. G. Elizarova and D. A. Saburin, “The numerical simulation of Faraday waves on the basis of hydrodynamic equations in the shallow-water approximation,” *Moscow Univ. Phys. Bull.* **70** (1), 1–6 (2015).
13. A. A. Zlotnik, “On construction of quasi-gasdynamical systems of equations and the barotropic system with the potential body force,” *Mat. Model.* **24** (4), 65–79 (2012).
14. A. A. Zlotnik, “Energy equalities and estimates for barotropic quasi-gasdynamical and quasi-hydrodynamic systems of equations,” *Comput. Math. Math. Phys.* **50** (2), 310–321 (2010).
15. A. A. Zlotnik and B. N. Chetverushkin, “Parabolicity of the quasi-gasdynamical system of equations, its hyperbolic second-order modification, and the stability of small perturbations for them,” *Comput. Math. Math. Phys.* **48** (3), 445–472 (2008).
16. A. A. Sukhomozgii and Yu. V. Sheretov, “Uniqueness of the solution of regularized Saint Venant equations in the linear approximation,” *Vestn. Tver. Gos. Univ., Ser. Prikl. Mat.*, No. 24, 5–7 (2012).
17. A. A. Sukhomozgii and Yu. V. Sheretov, “Testing a new algorithm for computing one-dimensional unsteady free surface flows,” *Vestn. Tver. Gos. Univ., Ser. Prikl. Mat.*, No. 27, 47–64 (2012).
18. T. G. Elizarova and O. V. Bulatov, Preprint No. 21, IPM RAN (Keldysh Institute of Applied Mathematics, Russian Academy of Sciences, Moscow, 2014).
19. T. G. Elizarova and M. A. Istomina, Preprint No. 65, IPM RAN (Keldysh Institute of Applied Mathematics, Russian Academy of Sciences, Moscow, 2014).
20. R. J. LeVeque, “Balancing source terms and flux gradients in high-resolution Godunov methods: The quasi-steady wave propagation algorithm,” *J. Comput. Phys.* **146** (1), 346–365 (1998).
21. Y. Huang, N. Zhang, and Y. Pei, “Well-balanced finite volume scheme for shallow water flooding and drying over arbitrary topography,” *Eng. Appl. Comput. Fluid Mech.* **7** (1), 40–54 (2013).
22. A. A. Zlotnik, “On conservative spatial discretizations of the barotropic quasi-gasdynamical system of equations with a potential body force,” *Comput. Math. Math. Phys.* **56** (2), 303–319 (2016).
23. M. Ricchiuto, R. Abgrall, and H. Deconinck, “Application of conservative residual distribution schemes to the solution of the shallow water equations on unstructured meshes,” *J. Comput. Phys.* **222**, 287–331 (2007).
24. A. Birman and J. Falcovitz, “Application of the GRP scheme to open channel flow equations,” *J. Comput. Phys.* **222**, 131–154 (2007).
25. A. S. Petrosyan, *Additional Topics in Hydrodynamics of Heavy Fluid with Free Surface*, Ser. Mechanics, Control, Informatics (Inst. Kosm. Issled. Ross. Akad. Nauk, Moscow, 2010) [in Russian].
26. Xu Kun, “A well-balanced gas-kinetic scheme for the shallow-water equations with source terms,” *J. Comput. Phys.* **178**, 533–562 (2002).
27. F. Marche, PhD Thesis (Universite de Bordeaux 1, 2005); www.math.u-bordeaux1.fr/marche/THESE/marche.pdf.
28. G. F. Carrier and H. P. Greenspan, “Water waves of finite amplitude on a sloping beach,” *J. Fluid Mech.* **4**, 97–109 (1958).
29. G. F. Carrier, T. T. Wu, and H. Yeh, “Tsunami run-up and draw-down on a plane beach,” *J. Fluid Mech.* **475**, 79–99 (2003).
30. Benchmark Problem 1: Tsunami Runup onto a plane beach; http://isec.nace.org/workshop/2004_cornell/bmark1.html.
31. NOAA Center for Tsunami Research. Tsunami Runup onto a Complex Three-dimensional Beach. Monai Valley; http://nctr.pmel.noaa.gov/benchmark/Laboratory/Laboratory_MonaiValley/index.html
32. M. Ricchiuto, “An explicit residual based approach for shallow water flows,” *J. Comput. Phys.* **280**, 306–344 (2015).

Translated by I. Ruzanova